

Cite this: *J. Mater. Chem. A*, 2024, 12, 20115

## Customized CO<sub>2</sub> electroreduction to methane or ethylene by manipulating \*H and \*CO adsorption on Cu/CeO<sub>x</sub> catalysts†

Tinghui Yang, Yingbing Zhang, Zichao Huang, Jianping Yang \* and Min Kuang \*

The coverage of \*CO and \*H intermediates on the surface of a catalyst plays a pivotal role in determining the selectivity towards C<sub>1</sub> or C<sub>2</sub> products in the electrochemical CO<sub>2</sub> reduction reaction (CO<sub>2</sub>RR). In this study, we engineered two types of interfaces involving copper and rare earth metal oxides, specifically Cu/CeO<sub>x</sub> and Cu/CuCeO<sub>x</sub> solid solution, which exhibit enhanced binding affinities for \*H and \*CO adsorbates in the CO<sub>2</sub>RR, respectively. As a result, the Cu/CuCeO<sub>x</sub> catalyst delivered an ethylene faradaic efficiency of 40.2% at a partial current density of −245.7 mA cm<sup>−2</sup>, whereas the Cu/CeO<sub>x</sub> catalyst presented a methane faradaic efficiency of 38.6% at a partial current density of −198.3 mA cm<sup>−2</sup>. Results of theoretical and experimental analyses have demonstrated that the Cu–Ce–O<sub>x</sub> solid solution markedly enhances \*CO adsorption by stabilizing Cu<sup>+</sup> species, thereby favoring its dimerization to ethylene rather than converting to methane through hydrogenation. This investigation elucidates a strategy for directing the selective electroproduction of C<sub>1</sub> or C<sub>2</sub> compounds from the CO<sub>2</sub>RR by effectively manipulating \*H and \*CO adsorption on Cu/CeO<sub>x</sub> catalysts.

Received 17th March 2024

Accepted 28th June 2024

DOI: 10.1039/d4ta01808g

rsc.li/materials-a

## Introduction

The relentless rise in atmospheric CO<sub>2</sub> levels, predominantly driven by anthropogenic activities, has been identified as a principal factor exacerbating global warming, eliciting widespread concern across the globe.<sup>1,2</sup> Within this critical context,

the electrochemical carbon dioxide reduction (CO<sub>2</sub>RR), especially when powered by renewable energy sources like solar and wind, has emerged as a vital strategy for carbon balance restoration.<sup>3–5</sup> Distinct from the generation of simpler C<sub>1</sub> products like formic acid (HCOOH) and carbon monoxide (CO),<sup>6</sup> there is an intensified demand for the production of high energy density hydrocarbons, notably methane (CH<sub>4</sub>) and ethylene (C<sub>2</sub>H<sub>4</sub>), which are envisioned as potential sustainable fuels.<sup>7–9</sup> To date, copper-based materials, endowed with optimal adsorption energy for the \*CO intermediate, have been heralded as the most effective catalysts for facilitating the conversion of CO<sub>2</sub> into valuable hydrocarbons.<sup>10,11</sup> In pursuit of this, a spectrum of Cu-based electrocatalysts, encompassing metallic Cu, Cu oxides,<sup>12–14</sup> Cu-integrated metal–organic frameworks (MOFs),<sup>15,16</sup> and Cu-centric molecules,<sup>17,18</sup> have been meticulously developed, marking significant strides in the electrocatalytic conversion of CO<sub>2</sub> to CH<sub>4</sub> or C<sub>2</sub>H<sub>4</sub>. Nevertheless, the design of cost-effective and durable catalysts tailored for the targeted transformation of CO<sub>2</sub> into high-energy products continues to pose a formidable challenge.

The mechanism underlying the CO<sub>2</sub>RR involves the initial reduction of CO<sub>2</sub> to adsorbed \*CO, succeeded by \*CO hydrogenation and/or C–C coupling processes.<sup>8,19</sup> Recent investigations have illuminated that \*CO hydrogenation to \*CHO represents the rate-limiting step in CH<sub>4</sub> generation, while \*CHO also acts as a pivotal intermediate for multi-carbon (C<sub>2</sub>) products.<sup>4,20</sup> Moreover, the journey from \*CO to hydrocarbons encapsulates a multi-step hydrogenation sequence, with \*H emerging as a crucial intermediary for hydrocarbon synthesis.

State Key Laboratory for Modification of Chemical Fibers and Polymer Materials, College of Materials Science and Engineering, Donghua University, Shanghai 201620, China. E-mail: jianpingyang@dhu.edu.cn; mkuang@dhu.edu.cn

† Electronic supplementary information (ESI) available. See DOI: <https://doi.org/10.1039/d4ta01808g>



Min Kuang

Min Kuang is currently a professor in the College of Materials Science and Engineering at Donghua University, China. She received her PhD from the Laboratory of Advanced Materials at Fudan University. Following this, she joined the School of Materials Science and Engineering at Nanyang Technological University as a post-doctoral research associate. Her research focuses on developing advanced electrochemical C<sub>1</sub>-to-

fuel conversion systems and exploring efficient electrocatalysts.

Consequently, fine-tuning the adsorption dynamics of  $^*CO$  and  $^*H$  presents a promising avenue for steering the  $CO_2RR$  towards desired products, particularly for  $CH_4$  and  $C_2H_4$ . For example, Zheng *et al.* showcased that the strategic incorporation of two metal dopants, Zn and Mn, into Cu matrices could simultaneously modulate the coverage of  $^*H$  and  $^*CO$ , enabling the fine-tuning of selectivity between  $CH_4$  and  $C_2H_4$ .<sup>21</sup> Similarly, Sargent *et al.* effectively manipulated  $^*CO$  coverage through varying  $CO_2$  concentrations, achieving tunable product specificity from  $C_2H_4$  to  $CH_4$ .<sup>22</sup> In a parallel vein, Wei and colleagues enhanced the adsorption of the CO intermediate by augmenting polyaniline on Cu substrates, thereby activating  $CO_2$  molecules and yielding a significant faradaic efficiency (FE) for  $C_2$  products.<sup>23</sup> Despite these advances, attaining high selectivity shifts between desired products using analogous materials remains elusive, thereby underscoring the impetus for novel catalyst development.

In this report, we introduce an innovative strategy employing functional rare-earth metal oxides to facilitate selectivity switching between  $CH_4$  and  $C_2H_4$  products by modulating  $^*H$  and  $^*CO$  adsorption (Fig. 1). Two distinct electrocatalysts, Cu/CeO<sub>x</sub> and a Cu/CuCeO<sub>x</sub> solid solution ( $0 < X < 2$ ), were synthesized, with the CeO<sub>x</sub> component enhancing  $^*H$  coverage through expedited water dissociation, while Cu–Ce–O<sub>x</sub> solid solutions stabilize Cu<sup>+</sup> species, augmenting  $^*CO$  adsorption and catalyzing the C–C coupling process. Electrochemical  $CO_2RR$  evaluations revealed that the Cu/CuCeO<sub>x</sub> catalyst achieved an ethylene FE of 40.2% at a partial current density of  $-245.7 \text{ mA cm}^{-2}$ , in contrast to the Cu/CeO<sub>x</sub> variant, which exhibited a methane FE of 38.6% at a partial current density of  $-198.3 \text{ mA cm}^{-2}$ . Density functional theory (DFT) calculations further illustrated that Cu–Ce–O<sub>x</sub> solid solutions significantly reduce the formation energy of the  $^*COCHO$  intermediate, thereby enhancing  $C_2H_4$  production. This paradigm of adjusting  $CO_2RR$  selectivity *via* intermediary coverage heralds new avenues for designing innovative Cu-based nanocomposite catalysts.

## Results and discussion

The Cu/CuCeO<sub>x</sub> catalyst was synthesized utilizing the coprecipitation methodology delineated in previous studies,<sup>24</sup> and subsequently subjected to annealing in a mixed atmosphere of 5 vol% H<sub>2</sub>/Ar (Fig. 2a and S1†). In contrast, the Cu/CeO<sub>x</sub> catalyst was fabricated through a bifurcated procedure: initially, CeO<sub>x</sub> was prepared devoid of any Cu precursor *via*

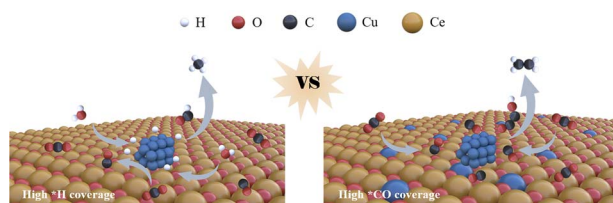


Fig. 1 Diagrams of methane and ethylene production on Cu/CeO<sub>x</sub> and Cu/CuCeO<sub>x</sub> during the  $CO_2RR$ , respectively.

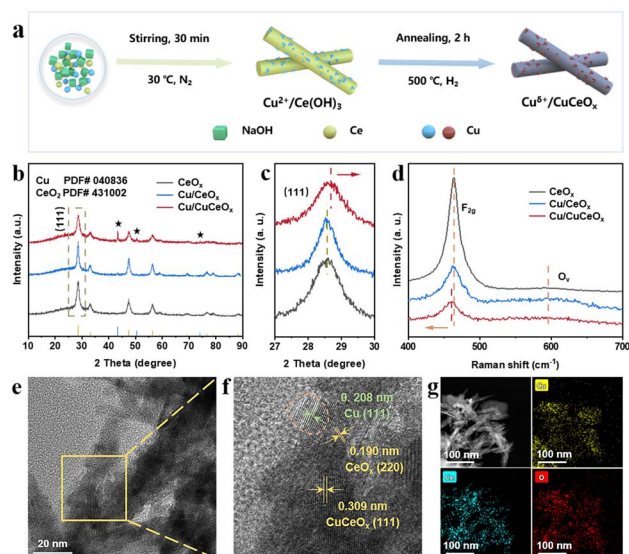


Fig. 2 (a) Synthetic route of the Cu/CuCeO<sub>x</sub> catalyst by a coprecipitation method. (b) XRD spectra, (c) local amplification of (111) and (d) Raman spectra for CeO<sub>x</sub>, Cu/CeO<sub>x</sub>, and Cu/CuCeO<sub>x</sub> catalysts (CeO<sub>2</sub>, yellow, PDF# 43-1002; Cu, blue, PDF# 04-0836). (e and f) HRTEM images and (g) EDX elemental distribution mapping images of Cu/CuCeO<sub>x</sub>.

coprecipitation; thereafter, Cu/CeO<sub>x</sub> was produced by an impregnation technique. The X-ray diffraction (XRD) analysis of the synthesized samples (Fig. 2b) reveals diffraction peaks at  $28.55^\circ$ ,  $32.08^\circ$ ,  $47.48^\circ$ ,  $56.34^\circ$ ,  $59.09^\circ$ ,  $69.42^\circ$ ,  $76.70^\circ$ ,  $79.08^\circ$ , and  $88.43^\circ$ , congruent with the established cubic fluorite-like structure of CeO<sub>2</sub> (PDF# 43-1002). Additionally, characteristic diffraction peaks of Cu are discernible (indicated by a pentagram at  $43.30^\circ$ ,  $50.43^\circ$ , and  $74.13^\circ$ ) corresponding to PDF# 04-0836. Notably, the (111) plane of Cu/CuCeO<sub>x</sub> exhibits a discernible shift towards higher Bragg angles compared to CeO<sub>x</sub> and Cu/CeO<sub>x</sub> (Fig. 2c), suggesting the formation of a Cu–Ce–O<sub>x</sub> solid solution due to the substitution of a larger cation by a smaller one.<sup>25–27</sup> As the Cu content continues to increase, some of the copper precipitates out, forming clustered copper species on the Cu/CuCeO<sub>x</sub> nanorods.<sup>28</sup> And no diffraction peaks corresponding to Cu can be found when the copper loading is below 30 wt%, which may be due to the high dispersion of Cu nanoparticles with too small particle sizes on the surface of the ceria support to be identified by the XRD (Fig. S2†).<sup>29,30</sup> Raman spectroscopy of the catalysts reveals an intense band around  $459 \text{ cm}^{-1}$  and another at approximately  $595 \text{ cm}^{-1}$ , corresponding to the  $F_{2g}$  vibration pattern and defect-induced mode ( $O_v$ ) in a cubic fluorite structure, respectively.<sup>31</sup> Notably, the  $F_{2g}$  bands of Cu/CuCeO<sub>x</sub> exhibit a redshift to lower frequencies with increasing Cu loading, compared to pure CeO<sub>x</sub> (Fig. S3†), indicative of Cu atom doping into the CeO<sub>x</sub> lattice and Cu/CuCeO<sub>x</sub> interface formation.<sup>32,33</sup> This results in extended Ce–O bond lengths at the interface and lattice distortions due to the atomic radius disparity between Cu<sup>+</sup> and Ce<sup>4+</sup>/Ce<sup>3+</sup>,<sup>34,35</sup> corroborating the XRD findings.

Transmission electron microscopy (TEM, Fig. S4†) images depict the Cu/CuCeO<sub>x</sub> as possessing rod-like nanostructures.

The dynamic light scattering in Fig. S5† further illustrates that the particle size distribution between 50 and 200 nm is slightly wider than that presented by TEM, which may be caused by partial rupture or aggregation of cerium dioxide. High-resolution TEM (HRTEM) images (Fig. 2e and f) identify the main interplanar spacings of 0.309 nm corresponding to the Cu–Ce–O<sub>x</sub> (111), slightly smaller than the Cu/CeO<sub>x</sub>'s CeO<sub>2</sub> (111) plane (0.312 nm) observed in Fig. S6.† Other characteristic *d*-spacings at 0.190 and 0.208 nm correspond to the CeO<sub>2</sub> (220) and Cu (111) planes, respectively. Elemental mapping *via* energy-dispersive X-ray spectroscopy (EDS, Fig. 2g) confirms the uniform distribution of Cu, Ce, and O within Cu/CuCeO<sub>x</sub> without significant agglomeration. Moreover, inductively coupled plasma atomic emission spectroscopy (ICP-OES) quantified the Ce and Cu composition, aligning closely with theoretical expectations (Table S1†).

The valence states and surface chemistry of Cu, Ce, and O were investigated by X-ray photoelectron spectroscopy (XPS). The Ce 3d XPS spectra for both Cu/CeO<sub>x</sub> and Cu/CuCeO<sub>x</sub> nanorods, depicted in Fig. 3a, were deconvoluted into eight peaks corresponding to Ce 3d<sub>5/2</sub> (*v*, 882.4 eV; *v'*, 884.9 eV; *v''*, 888.7 eV; *v'''*, 898.2 eV) and Ce 3d<sub>3/2</sub> states (*μ*, 900.8 eV; *μ'*, 903.5 eV; *μ''*, 907.2 eV; *μ'''*, 916.6 eV).<sup>36,37</sup> Peaks designated *v*, *v'*, *v''*, *μ*, *μ'*, and *μ'''* are indicative of Ce<sup>4+</sup> species, while the *v'* and *μ'* peaks are attributed to Ce<sup>3+</sup> species, denoting the coexistence of Ce<sup>4+</sup> and Ce<sup>3+</sup> within the composite matrix.<sup>38</sup> The relative abundance of Ce<sup>3+</sup> to total cerium species was quantitatively assessed and was summarized in Table S1.† The ratio of Ce<sup>3+</sup> in Cu/CeO<sub>x</sub> and Cu/CuCeO<sub>x</sub> is 0.114 and 0.128, respectively. A noteworthy observation was the positive shift in the Ce<sup>4+</sup> peaks for Cu/CuCeO<sub>x</sub> (Fig. S7†), suggestive of alterations in the central charge distribution between Cu and Ce.<sup>39</sup> The Cu/CuCeO<sub>x</sub> exhibited a predominance of Ce<sup>3+</sup> species, which are postulated to facilitate rapid electron transport and mitigate electron localization at the Cu<sup>2+</sup>/Cu<sup>+</sup> sites within the Cu–Ce–O<sub>x</sub> solid solution matrix.<sup>40</sup> The O 1s XPS spectra are analyzed in Fig. 3b,

which can be resolved into two distinct peaks by deconvolution: one at a lower binding energy of 529.3 eV associated with lattice oxygen (O<sub>latt</sub>) and another at 531.3 eV, ascribed to adsorbed oxygen species (O<sub>ads</sub>).<sup>41</sup> The number of oxygen vacancies calculated from the deconvoluted core level O 1s spectra is shown in Table S1.† The Cu 2p XPS spectra (Fig. 3c) exhibit binding energies of 952.7 eV and 932.9 eV, characteristic of Cu<sup>+</sup> or Cu<sup>0</sup> species.<sup>42,43</sup> A minor presence of CuO, attributed to inevitable surface oxidation, was also noted.<sup>39,44</sup> Given the challenges in distinguishing between Cu<sup>0</sup> and Cu<sup>+</sup> based on Cu 2p<sub>3/2</sub> spectra alone,<sup>29</sup> additional analysis was conducted using Cu LMM Auger kinetic energy spectra (Fig. 3d), where peaks at 570.0 and 565.3 eV substantiate the presence of Cu<sup>+</sup> and Cu<sup>0</sup> species, respectively.<sup>45,46</sup> Herein, most of the Cu on the surface is oxidized to monovalent Cu species. The Cu/CuCeO<sub>x</sub> sample possesses the most surface monovalent Cu species (0.78), much higher than that of Cu/CeO<sub>x</sub> (0.56). The presence of monovalent copper is conducive to the adsorption of \*CO.<sup>47</sup>

The CO<sub>2</sub>RR catalytic performances of Cu/CuCeO<sub>x</sub> catalysts were tested in a flow cell, in which 1.0 M KOH was used as the electrolyte. In this work, all the applied potentials were converted into a reversible hydrogen electrode (RHE) scale without *iR* correction. The linear sweep voltammetry curves (LSV) shown in Fig. 4a were recorded by feeding the CO<sub>2</sub> gas across the 1.0 M KOH interface. Note that the Cu/CuCeO<sub>x</sub> catalysts exhibited higher current density responses than those of CeO<sub>x</sub> and Cu/CeO<sub>x</sub> catalysts, and we assume that the formation of Cu–Ce–O<sub>x</sub> solid solutions may enrich active sites that kinetically favored the CO<sub>2</sub>RR. To verify the hypothesis, we conducted the cyclic voltammetry (CV) method to estimate the electrochemically active surface area (ECSA) of the catalysts (Fig. S8†). The results show that Cu/CuCeO<sub>x</sub> had larger ECSA values than the Cu/CeO<sub>x</sub> catalyst, indicating that the generation of Cu–Ce–O<sub>x</sub> solid

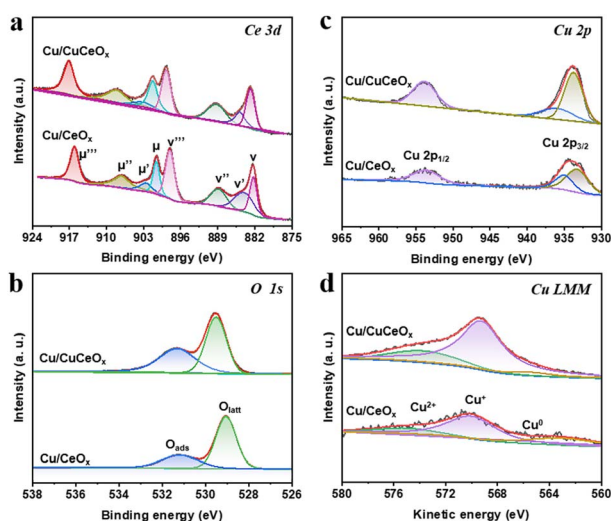


Fig. 3 XPS analysis of (a) Ce 3d, (b) O 1s, (c) Cu 2p, and (d) Cu LMM Auger spectra for Cu/CeO<sub>x</sub> and Cu/CuCeO<sub>x</sub>.

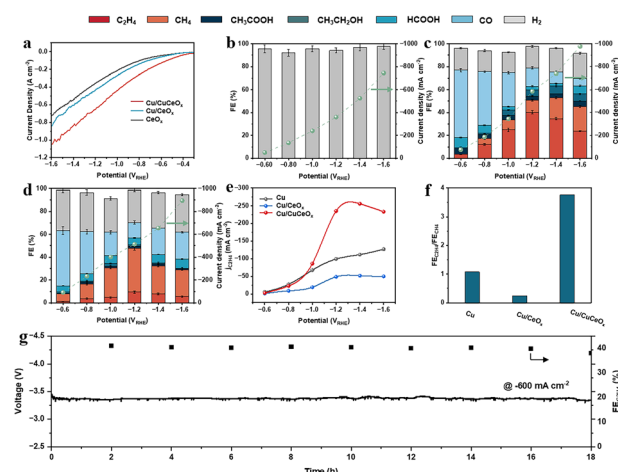


Fig. 4 (a) LSV spectra of CeO<sub>x</sub>, Cu/CeO<sub>x</sub>, and Cu/CuCeO<sub>x</sub> catalysts. (b–d) FEs of products at different applied potentials in 1.0 M KOH electrolyte for CeO<sub>x</sub>, Cu/CeO<sub>x</sub>, and Cu/CuCeO<sub>x</sub>. (e) C<sub>2</sub>H<sub>4</sub> partial current densities of Cu, Cu/CeO<sub>x</sub>, and Cu/CuCeO<sub>x</sub> under different potentials. (f) FE<sub>C<sub>2</sub>H<sub>4</sub></sub>/FE<sub>CH<sub>4</sub></sub> of CeO<sub>x</sub>, Cu/CeO<sub>x</sub>, and Cu/CuCeO<sub>x</sub> at –1.2 V<sub>RHE</sub>. (g) Stability test of Cu/CuCeO<sub>x</sub> during 18 h of long-time operation at –600 mA cm<sup>–2</sup>.

solutions favors the kinetics of the CO<sub>2</sub>RR *via* generating more interfacial active sites, which is consistent with the results of impedance analysis (Fig. S9†).

The gaseous and liquid products were quantitatively analyzed by on-line gas chromatography (GC, Fig. S10†) and <sup>1</sup>H nuclear magnetic resonance (<sup>1</sup>H NMR, Fig. S11†), respectively.<sup>48</sup> For the pure CeO<sub>2</sub> catalyst, H<sub>2</sub> was the main product (Fig. 4b). As shown in Fig. 4c, the Cu/CuCeO<sub>x</sub> catalyst exhibited a high FE<sub>C<sub>2</sub>H<sub>4</sub></sub> of 40.2% at  $-1.2$  V<sub>RHE</sub>. In comparison, the Cu and Cu/CeO<sub>x</sub> catalysts showed lower FE<sub>C<sub>2</sub>H<sub>4</sub></sub> at  $-1.2$  V<sub>RHE</sub> (Fig. 4d and S12†). For the pure Cu catalyst, the major products were H<sub>2</sub>, CH<sub>4</sub>, and C<sub>2</sub>H<sub>4</sub> species, while FE<sub>CH<sub>4</sub></sub> and FE<sub>C<sub>2</sub>H<sub>4</sub></sub> were 18.9% and 20.5%, respectively (Fig. S12†). In contrast, for the Cu/CeO<sub>x</sub> catalyst, CH<sub>4</sub> emerged as the predominant product, achieving a FE of 38.6% at a potential of  $-1.2$  V<sub>RHE</sub>. The comparison of FE for H<sub>2</sub> and the CH<sub>4</sub> products over those three catalysts further demonstrated that the formation of H<sub>2</sub> and the CH<sub>4</sub> species was suppressed on the Cu/CuCeO<sub>x</sub> catalyst. Furthermore, LSV measurements in an Ar-saturated 1.0 M KOH electrolyte without CO<sub>2</sub> gas revealed that CeO<sub>x</sub> exhibited the lowest overpotential at equivalent current densities, further affirming its proficiency in hydrogen evolution (Fig. S13†). Furthermore, the Cu/CuCeO<sub>x</sub> catalyst demonstrated the highest partial current density for C<sub>2</sub>H<sub>4</sub> production (Fig. 4e), signifying that Cu/CuCeO<sub>x</sub> has superior catalytic activity for C<sub>2</sub>H<sub>4</sub> synthesis compared to both pristine Cu and Cu/CeO<sub>x</sub>. Fig. 4f illustrates that the FE<sub>C<sub>2</sub>H<sub>4</sub></sub>/FE<sub>CH<sub>4</sub></sub> ratio achieved a maximum of 3.77 on Cu/CuCeO<sub>x</sub>, compared to 1.08 and 0.25 for Cu and Cu/CeO<sub>x</sub>, respectively, indicating that the formation of Cu–Ce–O<sub>x</sub> solid solutions is particularly conducive to C<sub>2</sub>H<sub>4</sub> production. Comparative electrochemical evaluations of Cu<sub>0.1</sub>/CuCeO<sub>x</sub> and Cu<sub>0.5</sub>/CuCeO<sub>x</sub>, synthesized *via* the same method, were also performed (Fig. S14†). A 50% increase in Cu loading led to a decline in C<sub>2</sub>H<sub>4</sub> selectivity, potentially due to the formation of larger Cu particles, which diminish the number of Cu active sites directly interacting with Ce, thereby inhibiting C–C coupling.<sup>36</sup> The long-term stability of Cu/CuCeO<sub>x</sub> was assessed through chronopotentiometry, and no significant decrease in Faraday efficiency of C<sub>2</sub>H<sub>4</sub> was observed during 18 h of electrocatalysis at  $-600$  mA cm<sup>-2</sup> (Fig. 4g). Post-CO<sub>2</sub>RR XPS analysis of the electrode confirmed the persistence of Cu<sup>+</sup> as the predominant valence state in Cu/CuCeO<sub>x</sub>, indirectly evidencing the stabilizing influence of the Cu–Ce–O<sub>x</sub> matrix on Cu<sup>+</sup> species (Fig. S15 and Table S1†). The efficient presence of Cu<sup>+</sup> was also demonstrated by *in situ* Raman spectra of a wide potential window (Fig. S16†), with characteristic peaks around 150, 230 and 500 cm<sup>-1</sup>.<sup>49,50</sup> Moreover, the characteristic peaks of the \*CO (2050 cm<sup>-1</sup>) intermediates were also observed, further indicating the high \*CO concentration on the Cu/CuCeO<sub>x</sub> catalyst surface.

Subsequent density functional theory (DFT) calculations were conducted for Cu/CeO<sub>x</sub> and Cu/CuCeO<sub>x</sub> catalysts to rationalize the effects of Cu–Ce–O<sub>x</sub> solid solutions on the CO<sub>2</sub>RR selectivity toward C<sub>2</sub>H<sub>4</sub> (Experimental section in the ESI, Fig. S17 and S18†). Initially, Bader charge analysis was applied to Cu/CuCeO<sub>x</sub> (Fig. 5a), revealing that copper integration into the cerium dioxide matrix diminished the charge density around the Cu sites, indicating that the charges of Cu and Ce were

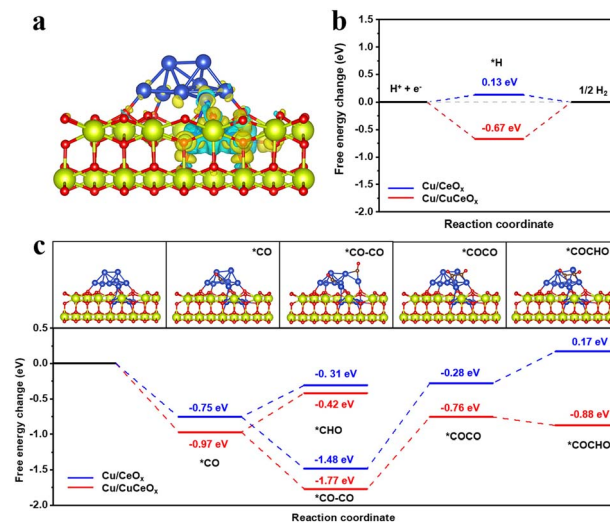


Fig. 5 (a) The Bader charge of Cu/CuCeO<sub>x</sub>. (b) Desorption energy diagram of hydrogen on Cu/CeO<sub>x</sub> and Cu/CuCeO<sub>x</sub>. (c) The free energy change diagram of \*CHO or \*COCHO generated by \*CO over the Cu/CeO<sub>x</sub> and Cu/CuCeO<sub>x</sub>.

rearranged.<sup>51</sup> The transfer of electrons from Cu to Ce<sup>3+</sup> results in higher Cu<sup>+</sup> in Cu/CuCeO<sub>x</sub>, which is conducive to promoting the adsorption of \*CO on the surface and enhancing C–C to achieve high selectivity of C<sub>2</sub>H<sub>4</sub>. This alteration favorably impacts the protonation of \*COCO intermediates, thereby facilitating C<sub>2</sub>H<sub>4</sub> formation. In addition, the hydrogen evolution reaction (HER) performance of both Cu/CeO<sub>x</sub> and Cu/CuCeO<sub>x</sub> was assessed (Fig. 5b). The Gibbs free energy ( $|\Delta G_{H^*}|$ ) for the HER on Cu/CeO<sub>x</sub> is 0.13 eV lower than that of Cu/CeCuO<sub>x</sub> (0.67 eV), thus allowing the promotion of the surface \*H coverage and the hydrogenation.

The free energy diagrams depicting the formation of \*CHO or \*COCHO from \*CO on the Cu/CeO<sub>x</sub> or Cu/CuCeO<sub>x</sub> catalysts are presented in Fig. 5c. Moreover, Cu/CuCeO<sub>x</sub> also exhibits significantly stronger \*CO adsorption than Cu/CeO<sub>x</sub>, enhancing the local \*CO concentration and favoring the C–C coupling process on the Cu/CeCuO<sub>x</sub> catalyst. According to previous reports,<sup>52</sup> the formation of CH<sub>4</sub> and C<sub>2</sub>H<sub>4</sub> is primarily governed by distinct rate-determining steps: the hydrogenation of \*CO to \*CHO for CH<sub>4</sub>, and the coupling of \*CO with \*CHO for C<sub>2</sub>H<sub>4</sub>, respectively.<sup>20,53</sup> For the Cu/CeO<sub>x</sub> catalyst, the  $\Delta G$  value of the CO hydrogenation is 0.44 eV lower than that of the Cu/CeCuO<sub>x</sub> catalyst, suggesting that Cu/CeO<sub>x</sub> has a higher selectivity for producing CH<sub>4</sub>. In contrast, the formation of the \*COCHO intermediate of the Cu/CuCeO<sub>x</sub> catalyst (0.12 eV) requires less free energy change than that of the Cu/CeO<sub>x</sub> catalyst (0.45 eV), indicating a more favorable C<sub>2</sub>H<sub>4</sub> pathway. Our computational findings corroborated that surfaces characterized by relatively high \*H and low \*CO coverage are conducive to the promotion of CH<sub>4</sub> production. Conversely, surfaces with a rich presence of \*CO and moderate levels of \*H are advantageous for the synthesis of C<sub>2</sub>H<sub>4</sub>.

Lastly, *in situ* infrared spectroscopy was employed to analyze potential surface intermediates on Cu/CeO<sub>x</sub> and Cu/CuCeO<sub>x</sub>

under various potential conditions, further elucidating the catalytic mechanism (Fig. S19†). Not only the peak of CO<sub>2</sub> can be observed in a pronounced absorption band of 2400–2300 cm<sup>-1</sup>,<sup>54,55</sup> but also the characteristic peak of CO (2050 cm<sup>-1</sup>) can also be identified,<sup>56</sup> which serves as evidence for the activation and reduction of CO<sub>2</sub>.<sup>57</sup> In addition, a distinct \*CHO peak, key intermediate for CH<sub>4</sub>, was further found at 1226 cm<sup>-1</sup>.<sup>58</sup> In contrast, in the Cu/CuCeO<sub>x</sub> spectrum, the characteristic peak of \*CHO is significantly weakened and replaced by \*COCHO at 1550 and 1185 cm<sup>-1</sup>,<sup>59–62</sup> indicating that Cu/CuCeO<sub>x</sub> catalysts are more inclined to produce C<sub>2</sub>, which is consistent with the results calculated by DFT.

## Conclusions

In summary, this study successfully demonstrates the selective electroreduction of CO<sub>2</sub> to CH<sub>4</sub> or C<sub>2</sub>H<sub>4</sub> by finely tuning \*H and \*CO adsorption on Cu/CeO<sub>x</sub> catalysts. Our innovative approach, involving the manipulation of Cu/CeO<sub>x</sub> and Cu/CuCeO<sub>x</sub> interfaces, significantly influences the catalytic selectivity towards desired C<sub>1</sub> or C<sub>2</sub> products. Notably, the Cu/CuCeO<sub>x</sub> electrocatalyst demonstrated a peak FE<sub>C<sub>2</sub>H<sub>4</sub></sub> of 40.2% and *j*<sub>C<sub>2</sub>H<sub>4</sub></sub> of -245.7 mA cm<sup>-2</sup>, while the Cu/CeO<sub>x</sub> electrocatalyst showed good CO<sub>2</sub>RR performances with a maximum FE<sub>CH<sub>4</sub></sub> of 38.6% and *j*<sub>CH<sub>4</sub></sub> of -198.3 mA cm<sup>-2</sup>. This advancement is underpinned by the enhanced \*CO adsorption facilitated by the stabilization of Cu<sup>+</sup> species within the Cu–Ce–O<sub>x</sub> solid solution. Our findings pave the way for the development of tailored catalysts capable of directing CO<sub>2</sub> electroreduction towards specific hydrocarbons, addressing critical needs in CO<sub>2</sub> mitigation and sustainable fuel production.

## Data availability

All the data supporting this article have been included in the main text and the ESI.†

## Author contributions

M. K. proposed, designed, and supervised the project. T. H., Y. B., Z. C., and J. P. wrote the manuscript. T. H., Y. B., and Z. C. performed the experiments and analyzed the data. All authors discussed the results and revised the manuscript.

## Conflicts of interest

The authors declare no conflicts of interest.

## Acknowledgements

This work was supported by the Shanghai Pujiang Program (22PJ1400200), the National Natural Science Foundation of China (no. 52122312 and 22209024), Tongcheng R&D Foundation (no. CPCIF-RA-0102), and the State Key Laboratory for Modification of Chemical Fibers and Polymer Materials, Donghua University.

## References

- 1 M. Li, F. Zhang, M. Kuang, Y. Ma, T. Liao, Z. Sun, W. Luo, W. Jiang and J. Yang, *Nano-Micro Lett.*, 2023, **15**, 238.
- 2 M. B. Ross, P. De Luna, Y. Li, C.-T. Dinh, D. Kim, P. Yang and E. H. Sargent, *Nat. Catal.*, 2019, **2**, 648.
- 3 Y. Ma, J. Wang, J. Yu, J. Zhou, X. Zhou, H. Li, Z. He, H. Long, Y. Wang, P. Lu, J. Yin, H. Sun, Z. Zhang and Z. Fan, *Matter*, 2021, **4**, 888.
- 4 W. Ma, S. Xie, T. Liu, Q. Fan, J. Ye, F. Sun, Z. Jiang, Q. Zhang, J. Cheng and Y. Wang, *Nat. Catal.*, 2020, **3**, 478.
- 5 H. Chen, Z. Wang, X. Wei, S. Liu, P. Guo, P. Han, H. Wang, J. Zhang, X. Lu and B. Wei, *Appl. Surf. Sci.*, 2021, **544**, 148965.
- 6 W. Ma, S. Xie, X.-G. Zhang, F. Sun, J. Kang, Z. Jiang, Q. Zhang, D.-Y. Wu and Y. Wang, *Nat. Commun.*, 2019, **10**, 892.
- 7 W. Zhu, L. Fan, Q. Geng, C. Wang, X. Fan, Y. Zhang and C. Li, *Chem. Eng. J.*, 2024, **489**, 151316.
- 8 S. Jin, Z. Hao, K. Zhang, Z. Yan and J. Chen, *Angew. Chem., Int. Ed.*, 2021, **60**, 20627–20648.
- 9 Q.-J. Wu, D.-H. Si, P.-P. Sun, Y.-L. Dong, S. Zheng, Q. Chen, S.-H. Ye, D. Sun, R. Cao and Y.-B. Huang, *Angew. Chem., Int. Ed.*, 2023, **62**, e202306822.
- 10 J. Zhang, C. Guo, S. Fang, X. Zhao, L. Li, H. Jiang, Z. Liu, Z. Fan, W. Xu, J. Xiao and M. Zhong, *Nat. Commun.*, 2023, **14**, 1298.
- 11 Z. Zhang, L. Bian, H. Tian, Y. Liu, Y. Bando, Y. Yamauchi and Z.-L. Wang, *Small*, 2022, **18**, 2107450.
- 12 H. Shi, L. Luo, C. Li, Y. Li, T. Zhang, Z. Liu, J. Cui, L. Gu, L. Zhang, Y. Hu, H. Li and C. Li, *Adv. Funct. Mater.*, 2024, **34**, 2310913.
- 13 Y. Sun, J. Xie, Z. Fu, H. Zhang, Y. Yao, Y. Zhou, X. Wang, S. Wang, X. Gao, Z. Tang, S. Li, X. Wang, K. Nie, Z. Yang and Y.-M. Yan, *ACS Nano*, 2023, **17**, 13974.
- 14 L. Ma, Q. Geng, L. Fan, J.-X. Li, D. Du, J. Bai and C. Li, *Nano Res.*, 2023, **16**, 9065–9072.
- 15 X. Xie, X. Zhang, M. Xie, L. Xiong, H. Sun, Y. Lu, Q. Mu, M. H. Rummeli, J. Xu, S. Li, J. Zhong, Z. Deng, B. Ma, T. Cheng, W. A. Goddard and Y. Peng, *Nat. Commun.*, 2022, **13**, 63.
- 16 T. Yan, P. Wang and W.-Y. Sun, *Small*, 2023, **19**, 2206070.
- 17 Q. Bie, H. Yin, Y. Wang, H. Su, Y. Peng and J. Li, *Chin. J. Catal.*, 2024, **57**, 96.
- 18 T. Zheng, C. Liu, C. Guo, M. Zhang, X. Li, Q. Jiang, W. Xue, H. Li, A. Li, C.-W. Pao, J. Xiao, C. Xia and J. Zeng, *Nat. Nanotechnol.*, 2021, **16**, 1386.
- 19 C. Chen, S. Yu, Y. Yang, S. Louisia, I. Roh, J. Jin, S. Chen, P.-C. Chen, Y. Shan and P. Yang, *Nat. Catal.*, 2022, **5**, 878.
- 20 J. Feng, L. Zhang, S. Liu, L. Xu, X. Ma, X. Tan, L. Wu, Q. Qian, T. Wu, J. Zhang, X. Sun and B. Han, *Nat. Commun.*, 2023, **14**, 4615.
- 21 Y. Chen, N. Lyu, J. Zhang, S. Yan, C. Peng, C. Yang, X. Lv, C. Hu, M. Kuang and G. Zheng, *Small*, 2024, 2308004.
- 22 X. Wang, A. Xu, F. Li, S.-F. Hung, D.-H. Nam, C. M. Gabardo, Z. Wang, Y. Xu, A. Ozden, A. S. Rasouli, A. H. Ip, D. Sinton and E. H. Sargent, *J. Am. Chem. Soc.*, 2020, **142**, 3525.
- 23 Q. Zhao, J. M. P. Martirez and E. A. Carter, *J. Am. Chem. Soc.*, 2021, **143**, 6152.

- 24 X. Guo, W. Ye, Z. a. Chen, A. Zhou, D. Jin and T. Ma, *Appl. Catal., B*, 2022, **310**, 121334.
- 25 W. Shan, W. Shen and C. Li, *Chem. Mater.*, 2003, **15**, 4761.
- 26 W. Liu, X. Liu, L. Feng, J. Guo, A. Xie, S. Wang, J. Zhang and Y. Yang, *Nanoscale*, 2014, **6**, 10693.
- 27 C.-A. Thieu, S. Yang, H.-I. Ji, H. Kim, K. J. Yoon, J.-H. Lee and J.-W. Son, *J. Mater. Chem. A*, 2022, **10**, 2460.
- 28 J. Jiang, H. Yang, H. Jiang, Y. Hu and C. Li, *Chem. Eng. J.*, 2023, **471**, 144439.
- 29 C. He, Y. Yu, L. Yue, N. Qiao, J. Li, Q. Shen, W. Yu, J. Chen and Z. Hao, *Appl. Catal., B*, 2014, **147**, 156.
- 30 P. Bera, K. R. Priolkar, P. R. Sarode, M. S. Hegde, S. Emura, R. Kumashiro and N. P. Lalla, *Chem. Mater.*, 2002, **14**, 3591.
- 31 B. Levasseur, A. M. Ebrahim and T. J. Bandosz, *Langmuir*, 2011, **27**, 9379.
- 32 T. Masui, K. Koyabu, K. Minami, T. Egawa and N. Imanaka, *J. Phys. Chem. C*, 2007, **111**, 13892.
- 33 S. Zhang, B. Jiang, M. Tong, Y. Yang, Z. Liao, Z. Huang, J. Sun, J. Wang and Y. Yang, *Ind. Eng. Chem. Res.*, 2023, **62**, 20667.
- 34 F. Jiang, S. Wang, B. Liu, J. Liu, L. Wang, Y. Xiao, Y. Xu and X. Liu, *ACS Catal.*, 2020, **10**, 11493.
- 35 H. Sun, H. Wang and Z. Qu, *ACS Catal.*, 2023, **13**, 1077.
- 36 S. Jin, D. Li, Z. Wang, Y. Wang, L. Sun and M. Zhu, *Catal. Sci. Technol.*, 2022, **12**, 7003.
- 37 M. Yusufoglu, S. Tafazoli, H. Jahangiri, M. B. Yağcı, T. Balkan and S. Kaya, *ACS Appl. Mater. Interfaces*, 2024, **16**, 7288.
- 38 C. W. Lee, S.-J. Shin, H. Jung, D. L. T. Nguyen, S. Y. Lee, W. H. Lee, D. H. Won, M. G. Kim, H.-S. Oh, T. Jang, H. Kim, B. K. Min and Y. J. Hwang, *ACS Energy Lett.*, 2019, **4**, 2241.
- 39 G. Tang, Y. Wu, J. Zhao, H. Zhang, M. Zhou and Y. Wang, *Chem.–Eur. J.*, 2022, **28**, e202103459.
- 40 Z. Yang, D. Ji, Z. Li, Z. He, Y. Hu, J. Yin, Y. Hou, P. Xi and C.-H. Yan, *Small*, 2023, **19**, 2303099.
- 41 W. Wang, Q. Zhu, F. Qin, Q. Dai and X. Wang, *Chem. Eng. J.*, 2018, **333**, 226.
- 42 R. Feng, Q. Zhu, M. Chu, S. Jia, J. Zhai, H. Wu, P. Wu and B. Han, *Green Chem.*, 2020, **22**, 7560.
- 43 J. Shan, Y. Shi, H. Li, Z. Chen, c. Sun, Y. Shuai and Z. Wang, *Chem. Eng. J.*, 2022, **433**, 133769.
- 44 K. Cao, H. Liu, W. Li, Q. Han, Z. Zhang, K. Huang, Q. Jing and L. Jiao, *Small*, 2019, **15**, 1901775.
- 45 S. Y. Lee, H. Jung, N.-K. Kim, H.-S. Oh, B. K. Min and Y. J. Hwang, *J. Am. Chem. Soc.*, 2018, **140**, 8681.
- 46 N. Martić, C. Reller, C. Macauley, M. Löffler, B. Schmid, D. Reinisch, E. Volkova, A. Maltenberger, A. Rucki, K. J. J. Mayrhofer and G. Schmid, *Adv. Energy Mater.*, 2019, **9**, 1901228.
- 47 B. Yang, W. Deng, L. Guo and T. Ishihara, *Chin. J. Catal.*, 2020, **41**, 1348–1359.
- 48 S. Liu, Y. Cao, H. Liu, H. Wang, B. Zhang, Y. Zhang, L. Zhang, S. Zhang and J. Sun, *Nanoscale*, 2021, **13**, 16986.
- 49 A. Xu, S.-F. Hung, A. Cao, Z. Wang, N. Karmodak, J. E. Huang, Y. Yan, A. Sedighian Rasouli, A. Ozden, F.-Y. Wu, Z.-Y. Lin, H.-J. Tsai, T.-J. Lee, F. Li, M. Luo, Y. Wang, X. Wang, J. Abed, Z. Wang, D.-H. Nam, Y. C. Li, A. H. Ip, D. Sinton, C. Dong and E. H. Sargent, *Nat. Catal.*, 2022, **5**, 1081–1088.
- 50 M. Wang, Z. Wang, Z. Huang, M. Fang, Y. Zhu and L. Jiang, *ACS Nano*, 2024, **18**, 15303–15311.
- 51 J. Zhang, P. Yu, C. Peng, X. Lv, Z. Liu, T. Cheng and G. Zheng, *ACS Catal.*, 2023, **13**, 7170.
- 52 L. Xiong, X. Zhang, L. Chen, Z. Deng, S. Han, Y. Chen, J. Zhong, H. Sun, Y. Lian, B. Yang, X. Yuan, H. Yu, Y. Liu, X. Yang, J. Guo, M. H. Rummeli, Y. Jiao and Y. Peng, *Adv. Mater.*, 2021, **33**, 2101741.
- 53 A. Vasileff, C. Xu, Y. Jiao, Y. Zheng and S. Z. Qiao, *Chem*, 2018, **4**, 1809.
- 54 G. N. Vayssilov, M. Mihaylov, P. S. Petkov, K. I. Hadjiivanov and K. M. Neyman, *J. Phys. Chem. C*, 2011, **115**, 23435.
- 55 Y. Yan, R. J. Wong, Z. Ma, F. Donat, S. Xi, S. Saqline, Q. Fan, Y. Du, A. Borgna, Q. He, C. R. Müller, W. Chen, A. A. Lapkin and W. Liu, *Appl. Catal., B*, 2022, **306**, 121098.
- 56 J. Yin, Z. Gao, F. Wei, C. Liu, J. Gong, J. Li, W. Li, L. Xiao, G. Wang, J. Lu and L. Zhuang, *ACS Catal.*, 2022, **12**, 1004.
- 57 Y. Katayama, F. Nattino, L. Giordano, J. Hwang, R. R. Rao, O. Andreussi, N. Marzari and Y. Shao-Horn, *J. Phys. Chem. C*, 2019, **123**, 5951.
- 58 P. Wang, H. Yang, C. Tang, Y. Wu, Y. Zheng, T. Cheng, K. Davey, X. Huang and S.-Z. Qiao, *Nat. Commun.*, 2022, **13**, 3754.
- 59 L. Zhang, J. Feng, L. Wu, X. Ma, X. Song, S. Jia, X. Tan, X. Jin, Q. Zhu, X. Kang, J. Ma, Q. Qian, L. Zheng, X. Sun and B. Han, *J. Am. Chem. Soc.*, 2023, **145**, 21945.
- 60 Q. Geng, L. Fan, H. Chen, C. Zhang, Z. Xu, Y. Tian, C. Yu, L. Kang, Y. Yamauchi, C. Li and L. Jiang, *J. Am. Chem. Soc.*, 2024, **146**, 10599–10607.
- 61 L. Fan, Q. Geng, L. Ma, C. Wang, J.-X. Li, W. Zhu, R. Shao, W. Li, X. Feng, Y. Yamauchi, C. Li and L. Jiang, *Chem. Sci.*, 2023, **14**, 13851–13859.
- 62 S. Hu, Y. Chen, Z. Zhang, S. Li, H. Liu, X. Kang, J. Liu, S. Ge, J. Wang, W. Lv, Z. Zeng, X. Zou, Q. Yu and B. Liu, *Small*, 2024, **20**, 2308226.